30. III–V Ternary and Quaternary Compounds

Sadao Adachi

III–V ternary and quaternary alloy systems are potentially of great importance for many high–speed electronic and optoelectronic devices, because they provide a natural means of tuning the magnitude of forbidden gaps so as to optimize and widen the applications of such semiconductor devices. Literature on the fundamental properties of these material systems is growing rapidly. Even though the basic semiconductor alloy concepts are understood at this time, some practical and device parameters in these material systems have been hampered by a lack of definite knowledge of many material parameters and properties.

This chapter attempts to summarize, in graphical and tabular forms, most of the important theoretical and experimental data on the III–V ternary and quaternary alloy parameters and properties. They can be classified into six groups:

1. Structural parameters
2. Mechanical, elastic, and lattice vibronic properties
3. Thermal properties
4. Energy band parameters
5. Optical properties
6. Carrier transport properties.

The III–V ternary and quaternary alloys considered here are those of Group III (Al, Ga, In) and V (N, P, As, Sb) atoms. The model used in some cases is based on an interpolation scheme and, therefore, requires that data on the material parameters for the related binaries (AlN, AlP, GaN, GaP, etc.) are known. These data have been taken mainly from the Landolt–Börnstein collection, Vol. III/41, and from the *Handbook on Physical Properties of Semiconductors Volume 2: III–V Compound Semiconductors*, published by Springer in 2004. The material parameters and properties derived here are used with wide success to obtain the general properties of these alloy semiconductors.

30.1 Introduction to III–V Ternary and Quaternary Compounds

III–V semiconducting compound alloys are widely used as materials for optoelectronic devices such as light-emitting diodes, laser diodes and photodetectors, as well as for electronic transport devices such as field effect transistors, high electron mobility transistors and heterojunction bipolar transistors. In a ternary alloy, the bandgap energy E_g and the lattice parameter a are generally both functions of a single composition parameter, so they cannot be selected independently. In quaternary alloys, on the other hand, the two composition parameters allow E_g and a to be selected independently, within the constraints of a given alloy-substrate system. Even though the basic semiconductor alloy concepts are understood at this time, the determination of some practical device parameters has been hampered by a lack of definite knowledge of many material parameters. This chapter provides data on the fundamental material properties of III–V ternary and quaternary alloys. The model used here is based on an interpolation scheme and thus requires that values of the material parameters for the related endpoint binaries are known. We therefore begin with the constituent binaries and gradually move on to alloys. The phenomenon of spontaneous ordering in semiconductor alloys, which can be categorized as a self-organized process, is observed to occur spontaneously during the epitaxial growth of certain alloys, and results in modifications to their structural, electronic and optical properties. This topic is omitted from the coverage [30.1].

30.2 Interpolation Scheme

The electronic energy band parameters of III–V compound alloys and their dependence on alloy composition are very important device parameters, and so they have received considerable attention in the past. Investigations of many device parameters have, however, been hampered by a lack of definite knowledge of various material parameters. This necessitates the use of some kind of interpolation scheme. Although the interpolation scheme is still open to experimental verification, it can provide more useful and reliable material parameters over the entire range of alloy composition [30.2].

If one uses the linear interpolation scheme, the ternary parameter T can be derived from the binary parameters (B) by

$$T_{A_xB_{1-x}C} = xB_{AC} + (1-x)B_{BC} \equiv a + bx \quad (30.1)$$

for an alloy of the form $A_xB_{1-x}C$, where $a \equiv B_{BC}$ and $b \equiv B_{AC} - B_{BC}$. Some material parameters, however, deviate significantly from the linear relation (30.1), and exhibit an approximately quadratic dependence on the mole fraction x. The ternary material parameter in such a case can be very efficiently approximated by the relationship

$$T_{A_xB_{1-x}C} = xB_{AC} + (1-x)B_{BC} + C_{A-B}x(1-x)$$
$$\equiv a + bx + cx^2 , \quad (30.2)$$

where $a \equiv B_{BC}$ and $b \equiv B_{AC} - B_{BC} + C_{A-B}$, and $c \equiv -C_{A-B}$. The parameter c is called the bowing or nonlinear parameter.

The quaternary material $A_xB_{1-x}C_yD_{1-y}$ is thought to be constructed from four binaries: AC, AD, BC, and BD. If one uses the linear interpolation scheme, the quaternary parameter Q can be derived from the Bs by

$$Q(x, y) = xyB_{AC} + x(1-y)B_{AD} + (1-x)yB_{BC} + (1-x)(1-y)B_{BD} . \quad (30.3)$$

If one of the four binary parameters (e.g., B_{AD}) is lacking, Q can be estimated from

$$Q(x, y) = xB_{AC} + (y-x)B_{BC} + (1-y)B_{BD} . \quad (30.4)$$

The quaternary material $A_xB_yC_{1-x-y}D$ is thought to be constructed from three binaries: AD, BD, and CD. The corresponding linear interpolation is given by

$$Q(x, y) = xB_{AD} + yB_{BD} + (1-x-y)B_{CD} . \quad (30.5)$$

If the material parameter can be given by a specific expression owing to some physical basis, it is natural to consider that the interpolation scheme may also obey this expression. The static dielectric constant ε_s is just the case that follows the Clausius–Mosotti relation. Then, the interpolation expression for the $A_xB_{1-x}C_yD_{1-y}$ quaternary, for example, has the

form

$$\frac{\varepsilon_s(x,y)-1}{\varepsilon_s(x,y)-2} = xy\frac{\varepsilon_s(AC)-1}{\varepsilon_s(AC)-2} + x(1-y)\frac{\varepsilon_s(AD)-1}{\varepsilon_s(AD)-2}$$
$$+ (1-x)y\frac{\varepsilon_s(BC)-1}{\varepsilon_s(BC)-2}$$
$$+ (1-x)(1-y)\frac{\varepsilon_s(BD)-1}{\varepsilon_s(BD)-2} \, .$$

$$(30.6)$$

When bowing from the anion sublattice disorder is independent of the disorder in the cation sublattice, the interpolation scheme is written by incorporating these cation and anion bowing parameters into the linear interpolation scheme as

$$Q(x,y) = xyB_{AC} + x(1-y)B_{AD} + (1-x)yB_{BC}$$
$$+ (1-x)(1-y)B_{BD} + C_{A-B}x(1-x)$$
$$+ C_{C-D}y(1-y)$$

$$(30.7)$$

for the $A_xB_{1-x}C_yD_{1-y}$ quaternary, or

$$Q(x,y) = xB_{AD} + yB_{BD} + (1-x-y)B_{CD}$$
$$+ C_{A-B-C}xy(1-x-y)$$
$$(30.8)$$

for the $A_xB_yC_{1-x-y}D$ quaternary.

30.3 Structural Parameters

30.3.1 Lattice Parameters and Lattice-Matching Conditions Between III–V Quaternaries and Binary Substrates

The lattice parameter a (c) is known to obey Vegard's law well, i.e., to vary linearly with composition. Thus, the lattice parameter for a III–V ternary can be simply obtained from (30.1) using the binary data listed in Table 30.1 [30.3, 4]. Introducing the lattice parameters in Table 30.1 into (30.3) [(30.5)], one can also obtain the lattice-matching conditions for $A_{1-x}B_xC_yD_{1-y}$ $(A_xB_yC_{1-x-y}D)$ quaternaries on various III–V binary substrates (GaAs, GaSb, InP and InAs). These results are summarized in Tables 30.2, 30.3, 30.4 and 30.5.

30.3.2 Molecular and Crystal Densities

The molecular density d_M can be obtained via

$$d_M = \frac{4}{a^3} \qquad (30.12)$$

for zinc blende-type materials, and

$$d_M = \frac{4}{a_{eff}^3} \qquad (30.13)$$

If relationships for the ternary parameters Ts are available, the quaternary parameter Q can be expressed either as ($A_xB_{1-x}C_yD_{1-y}$)

$$Q(x,y) = \frac{x(1-x)[yT_{ABC}(x) + (1-y)T_{ABD}(x)]}{x(1-x)+y(1-y)}$$
$$+ \frac{y(1-y)[xT_{ACD}(y) + (1-x)T_{BCD}(y)]}{x(1-x)+y(1-y)} \, ,$$

$$(30.9)$$

or ($A_xB_yC_{1-x-y}D$)

$$Q(x,y) = \frac{xyT_{ABD}(u) + y(1-x-y)T_{BCD}(v)}{xy+y(1-x-y)+x(1-x-y)}$$
$$+ \frac{x(1-x-y)T_{ACD}(w)}{xy+y(1-x-y)+x(1-x-y)}$$

$$(30.10)$$

with

$$u = \frac{1}{2}(1-x-y) \, ,$$
$$v = \frac{1}{2}(2-x-2y) \, ,$$
$$w = \frac{1}{2}(2-2x-y) \, .$$

$$(30.11)$$

for wurtzite-type materials, where a_{eff} is an effective cubic lattice parameter defined by

$$a_{eff} = \left(\sqrt{3}a^2c\right)^{1/3} \, . \qquad (30.14)$$

Table 30.1 Lattice parameters a and c and crystal density g for some III–V binaries at 300 K

Binary	Zinc blende	Wurtzite		g
	a (Å)	a (Å)	c (Å)	(g/cm^{-3})
AlN	–	3.112	4.982	3.258
	4.38	–	–	3.24
AlP	5.4635	–	–	2.3604
AlAs	5.66139	–	–	3.7302
AlSb	6.1355	–	–	4.2775
α-GaN	–	3.1896	5.1855	6.0865
β-GaN	4.52	–	–	6.02
GaP	5.4508	–	–	4.1299
GaAs	5.65330	–	–	5.3175
GaSb	6.09593	–	–	5.6146
InN	–	3.548	5.760	6.813
	4.986	–	–	6.903
InP	5.8690	–	–	4.7902
InAs	6.0583	–	–	5.6678
InSb	6.47937	–	–	5.7768

Table 30.2 Lattice-matching conditions for some III–V quaternaries of type $A_xB_{1-x}C_yD_{1-y}$ at 300 K. $x = \frac{A_0 + B_0 y}{C_0 + D_0 y}$

Quaternary	Substrate	A_0	B_0	C_0	D_0	Remark
$Ga_xIn_{1-x}P_yAs_{1-y}$	GaAs	0.4050	−0.1893	0.4050	0.0132	$0 \le y \le 1.0$
	InP	0.1893	−0.1893	0.4050	0.0132	$0 \le y \le 1.0$
$Al_xIn_{1-x}P_yAs_{1-y}$	GaAs	0.4050	−0.1893	0.3969	0.0086	$0.04 \le y \le 1.0$
	InP	0.1893	−0.1893	0.3969	0.0086	$0 \le y \le 1.0$

Table 30.3 Lattice-matching conditions for some III–V quaternaries of type $A_xB_{1-x}C_yD_{1-y}$ at 300 K. $y = \frac{A_0 + B_0 x}{C_0 + D_0 x}$

Quaternary	Substrate	A_0	B_0	C_0	D_0	Remark
$Al_xGa_{1-x}P_yAs_{1-y}$	GaAs	0	0.0081	0.2025	−0.0046	$0 \le x \le 1.0$
$Al_xGa_{1-x}As_ySb_{1-y}$	GaSb	0	0.0396	0.4426	0.0315	$0 \le x \le 1.0$
	InP	0.2269	0.0396	0.4426	0.0315	$0 \le x \le 1.0$
	InAs	0.0376	0.0396	0.4426	0.0315	$0 \le x \le 1.0$
$Al_xGa_{1-x}P_ySb_{1-y}$	GaAs	0.4426	0.0396	0.6451	0.0269	$0 \le x \le 1.0$
	GaSb	0	0.0396	0.6451	0.0269	$0 \le x \le 1.0$
	InP	0.2269	0.0396	0.6451	0.0269	$0 \le x \le 1.0$
	InAs	0.0376	0.0396	0.6451	0.0269	$0 \le x \le 1.0$
$Ga_xIn_{1-x}As_ySb_{1-y}$	GaSb	0.3834	−0.3834	0.4211	0.0216	$0 \le x \le 1.0$
	InP	0.6104	−0.3834	0.4211	0.0216	$0.47 \le x \le 1.0$
	InAs	0.4211	−0.3834	0.4211	0.0216	$0 \le x \le 1.0$
$Ga_xIn_{1-x}P_ySb_{1-y}$	GaAs	0.8261	−0.3834	0.6104	0.0348	$0.52 \le x \le 1.0$
	GaSb	0.3834	−0.3834	0.6104	0.0348	$0 \le x \le 1.0$
	InP	0.6104	−0.3834	0.6104	0.0348	$0 \le x \le 1.0$
	InAs	0.4211	−0.3834	0.6104	0.0348	$0 \le x \le 1.0$
$Al_xIn_{1-x}As_ySb_{1-y}$	GaSb	0.3834	−0.3439	0.4211	0.0530	$0 \le x \le 1.0$
	InP	0.6104	−0.3439	0.4211	0.0530	$0.48 \le x \le 1.0$
	InAs	0.4211	−0.3439	0.4211	0.0530	$0 \le x \le 1.0$
$Al_xIn_{1-x}P_ySb_{1-y}$	GaAs	0.8261	−0.3439	0.6104	0.0616	$0.53 \le x \le 1.0$
	GaSb	0.3834	−0.3439	0.6104	0.0616	$0 \le x \le 1.0$
	InP	0.6104	−0.3439	0.6104	0.0616	$0 \le x \le 1.0$
	InAs	0.4211	−0.3439	0.6104	0.0616	$0 \le x \le 1.0$

Table 30.4 Lattice-matching conditions for some III–V quaternaries of type $A_xB_yC_{1-x-y}D$ at 300 K. $y = A_0 + B_0 x$

Quaternary	Substrate	A_0	B_0	Remark
$Al_xGa_yIn_{1-x-y}P$	GaAs	0.5158	−0.9696	$0 \le x \le 0.53$
$Al_xGa_yIn_{1-x-y}As$	InP	0.4674	−0.9800	$0 \le x \le 0.48$

Table 30.5 Lattice-matching conditions for some III–V quaternaries of type $AB_xC_yD_{1-x-y}$ at 300 K. $x = A_0 + B_0 y$

Quaternary	Substrate	A_0	B_0	Remark
$AlP_xAs_ySb_{1-x-y}$	GaAs	0.7176	−0.7055	$0 \le y \le 1.0$
	InP	0.3966	−0.7055	$0 \le y \le 0.56$
	InAs	0.1149	−0.7055	$0 \le y \le 0.16$
$GaP_xAs_ySb_{1-x-y}$	GaAs	0.6861	−0.6861	$0 \le y \le 1.0$
	InP	0.3518	−0.6861	$0 \le y \le 0.51$
	InAs	0.0583	−0.6861	$0 \le y \le 0.085$
$InP_xAs_ySb_{1-x-y}$	GaSb	0.6282	−0.6899	$0 \le y \le 0.911$
	InAs	0.6899	−0.6899	$0 \le y \le 1.0$

The x-ray crystal density g can be simply written, using d_M, as

$$g = \frac{M d_M}{N_A}, \tag{30.15}$$

where M is the molecular weight and $N_A = 6.022 \times 10^{23}\ \mathrm{mol}^{-1}$ is the Avogadro constant. We list g for some III–V binaries in Table 30.1. Alloy values of d_M and g can be accurately obtained using Vegard's law, i. e., (30.1), (30.3), and (30.5).

30.4 Mechanical, Elastic and Lattice Vibronic Properties

30.4.1 Microhardness

The hardness test has been used for a long time as a simple means of characterizing the mechanical behavior of solids. The Knoop hardness H_P for $Ga_xIn_{1-x}P_yAs_{1-y}$ lattice-matched to InP has been reported [30.5], and is found to increase gradually from $520 \, kg/mm^2$ for $y = 0$ ($Ga_{0.47}In_{0.53}As$) to $380 \, kg/mm^2$ for $y = 1.0$ (InP). It has also been reported that the microhardness in $Al_xGa_{1-x}N$ thin film slightly decreases with increasing AlN composition x [30.6].

30.4.2 Elastic Constants and Related Moduli

Although the elastic properties of the III–V binaries have been studied extensively, little is known about their alloys. Recent studies, however, suggested that the elastic properties of the alloys can be obtained, to a good approximation, by averaging the binary end-point values [30.7, 8]. We have, therefore, listed in Tables 30.6 and 30.7 the elastic stiffness (C_{ij}) and compliance constants (S_{ij}) for some III–V binaries with zinc blende and wurtzite structures, respectively. Table 30.8 also summarizes the functional expressions for the bulk modulus B_u, Young's modulus Y, and Poisson's ratio P.

Note that Y and P are not isotropic, even in the cubic zinc blende lattice.

30.4.3 Long–Wavelength Phonons

The atoms of a crystal can be visualized as being joined by harmonic springs, and the crystal dynamics can be analyzed in terms of a linear combination of $3N$ normal modes of vibration (N is the number of different types of atoms; different in terms of mass or ordering in space). In alloys, the nature of the lattice optical spectrum depends on the difference between the quantities representing the lattice vibronic properties of the components. If these quantities are similar, then the optical response of an alloy is similar to the response of a crystal with the quantities averaged over the composition (one-mode behavior). In one-mode systems, such as most I–VII alloys, a single set of long-wavelength optical modes appears, as schematically shown in Fig. 30.1. When the parameters differ strongly, the response of a system is more complex; the spectrum contains a number of bands, each of which corresponds to one of the components, and it has an intensity governed by its content in the alloy (*multimode behavior*). For example, a two-mode system exhibits

Table 30.6 Elastic stiffness (C_{ij}) and compliance constants (S_{ij}) for some cubic III–V binaries at 300 K

Binary	C_{ij} (10^{11} dyn/cm^2)			S_{ij} (10^{-12} cm^2/dyn)		
	C_{11}	C_{12}	C_{44}	S_{11}	S_{12}	S_{44}
AlN	31.5[a]	15.0[a]	18.5[a]	0.458[a]	−0.148[a]	0.541[a]
AlP	15.0[a]	6.42[a]	6.11[a]	0.897[a]	−0.269[a]	1.64[a]
AlAs	11.93	5.72	5.72	1.216	−0.394	1.748
AlSb	8.769	4.341	4.076	1.697	−0.5618	2.453
β-GaN	29.1[a]	14.8[a]	15.8[a]	0.523[a]	−0.176[a]	0.633[a]
GaP	14.050	6.203	7.033	0.9756	−0.2988	1.422
GaAs	11.88	5.38	5.94	1.173	−0.366	1.684
GaSb	8.838	4.027	4.320	1.583	−0.4955	2.315
InN	19.2[a]	7.30[a]	9.35[a]	0.659[a]	−0.182[a]	1.07[a]
InP	10.22	5.73	4.42	1.639	−0.589	2.26
InAs	8.329	4.526	3.959	1.945	−0.6847	2.526
InSb	6.608	3.531	3.027	2.410	−0.8395	3.304

[a] Theoretical

Table 30.7 Elastic stiffness (C_{ij}) and compliance constants (S_{ij}) for some wurtzite III–V binaries at 300 K

Binary	C_{ij} (10^{11} dyn/cm^2)						S_{ij} (10^{-12} cm^2/dyn)					
	C_{11}	C_{12}	C_{13}	C_{33}	C_{44}	C_{66}^a	S_{11}	S_{12}	S_{13}	S_{33}	S_{44}	S_{66}^b
AlN	41.0	14.0	10.0	39.0	12.0	13.5	0.285	−0.085	−0.051	0.283	0.833	0.740
α-GaN	37.3	14.1	8.0	38.7	9.4	11.6	0.320	−0.112	−0.043	0.276	1.06	0.864
InN	19.0	10.4	12.1	18.2	0.99	4.3	0.957	−0.206	−0.499	1.21	10.1	2.33

$^aC_{66} = 1/2(C_{11} - C_{12})$, $^bS_{66} = 2(S_{11} - S_{12})$

Table 30.8 Functional expressions for the bulk modulus B_u, Young's modulus Y, and Poisson's ratio P in semiconductors with zinc blende (ZB) and wurtzite (W) structures

Parameter	Structure	Expression	Remark
B_u	ZB	$(C_{11} + 2C_{12})/3$	
	W	$[(C_{11} + C_{12})C_{33} - 2C_{13}^2]/(C_{11} + C_{12} + 2C_{33} - 4C_{13})$	
Y	ZB	$1/S_{11}$	(100), [001]
		$1/(S_{11} - S/2)$	(100), [011]
		$1/S_{11}$	(110), [001]
		$1/(S_{11} - 2S/3)$	(110), [111]
		$1/(S_{11} - S/2)$	(111)
	W	$1/S_{11}$	$c \perp l$
		$1/S_{33}$	$c \parallel l$
P	ZB	$-S_{12}/S_{11}$	(100), $m = [010]$, $n = [001]$
		$-(S_{12} + S/2)/(S_{11} - S/2)$	(100), $m = [011]$, $n = [0\bar{1}1]$
		$-S_{12}/S_{11}$	(110), $m = [001]$, $n = [1\bar{1}0]$
		$-(S_{12} + S/3)/(S_{11} - 2S/3)$	(110), $m = [1\bar{1}1]$, $n = [1\bar{1}\bar{2}]$
		$-(S_{12} + S/6)/(S_{11} - S/2)$	(111)
	W	$(1/2)[1 - (Y/3B_u)]$	$c \perp l, c \parallel l$

$S = S_{11} - S_{12} - (S_{44}/2)$; l = directional vector; m = direction for a longitudinal stress; n = direction for a transverse strain ($n \perp m$)
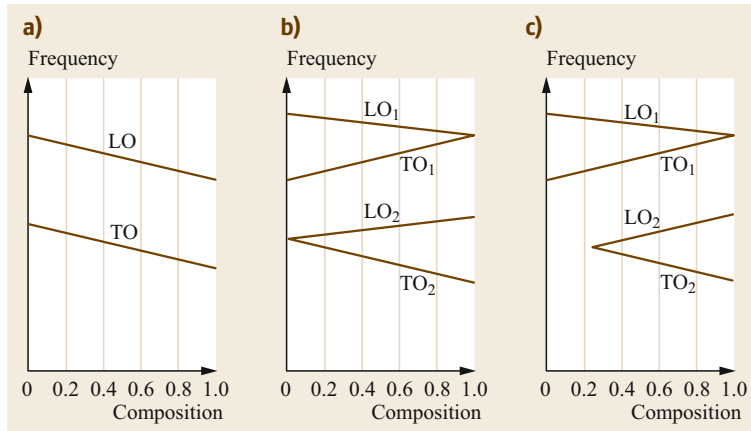
Fig. 30.1a–c Three different types of long-wavelength phonon mode behavior in ternary alloys: **(a)** one-mode; **(b)** two-mode; and **(c)** one–two-mode

Table 30.9 Behavior of the long-wavelength optical modes in III–V ternary and quaternary alloys

Behavior	Alloy
One mode	AlGaN (LO; cubic), AlGaN (except for E_1(TO); wurtzite), GaInN, AlAsSb
Two mode	AlGaN (TO; cubic), AlGaN (E_1(TO); wurtzite), AlInN, AlGaP, AlGaAs, AlGaSb, AlInP, AlInAs, AlInSb, GaInP, GaInAs, GaNP, GaNAs, GaPAs, GaPSb, GaAsSb, InPAs, InPSb
One–two mode	GaInSb, InAsSb
Two–three mode	AlGaInP/GaAs
Three mode	AlGaAsSb, GaInAsSb, AlGaInAs/InP, InPAsSb
Three–four mode	AlGaPAs
Four mode	GaInPSb, GaInPAs/GaAs, GaInPAs/InP

two distinct sets of optical modes with frequencies characteristic of each end member and strengths that are roughly proportional to the respective concentrations.

As seen in Table 30.9, the long-wavelength optical phonons in III–V ternaries exhibit either one-mode or two-mode behavior, or more rigorously, three different types of mode behavior: one-mode, two-mode, and one–two-mode behaviors. The one–two-mode system exhibits a single mode over only a part of the composition range, with two modes observed over the remaining range of compositions.

In a quaternary alloy of the $A_xB_{1-x}C_yD_{1-y}$ type, there are four kinds of unit cells: AC, AD, BC, and BD. On the other hand, in the $A_xB_yC_{1-x-y}D$ type there are three kinds of unit cells: AD, BD, and CD. We can, thus, expect four-mode or three-mode behavior of the long-wavelength optical modes in such quaternary alloys ([30.9]; Table 30.9). However, the $Ga_xIn_{1-x}As_ySb_{1-y}$ quaternary showed three-mode behavior with GaAs, InSb and mixed InAs/GaAs characteristics [30.10]. The $Ga_xIn_{1-x}As_ySb_{1-y}$ quaternary was also reported to show two-mode or three-mode behavior, depending on the alloy composition [30.11].

The long-wavelength optical phonon behavior in the $Al_xGa_{1-x}As$ ternary has been studied both theoretically and experimentally. These studies suggest that the optical phonons in $Al_xGa_{1-x}As$ exhibit the two-mode behavior over the whole composition range. Thus, the $Al_xGa_{1-x}As$ system has two couples of the transverse optical (TO) and longitudinal optical (LO) modes; one is the GaAs-like mode and the other is the AlAs-like mode. Each phonon frequency can be expressed as [30.12]:

- TO (GaAs): $268 - 14x$ cm^{-1}
- LO (GaAs): $292 - 38x$ cm^{-1}
- TO (AlAs): $358 + 4x$ cm^{-1}
- LO (AlAs): $358 + 71x - 26x^2$ cm^{-1}.

It is observed that only the AlAs-like LO mode shows a weak nonlinearity with respect to the alloy composition x.

30.5 Thermal Properties

30.5.1 Specific Heat and Debye Temperature

Since alloying has no significant effect on elastic properties, it appears that using the linear interpolation scheme for alloys can provide generally acceptable specific heat values (C). In fact, it has been reported that the C values for InP_xAs_{1-x} [30.13] and $Al_xGa_{1-x}As$ [30.14] vary fairly linearly with alloy composition x. It has also been shown [30.12] that the Debye temperature θ_D for alloys shows very weak nonlinearity with composition. From these facts, one can suppose that the linear interpolation scheme may provide generally acceptable C and θ_D values for III–V semiconductor alloys. We have, therefore, listed in Table 30.10 the III–V binary endpoint values for C and θ_D at $T = 300$ K. Using these values, the linearly interpolated C value for $Al_xGa_{1-x}As$ can be obtained from $C(x) = 0.424x + 0.327(1 - x) = 0.327 + 0.097x$ (J/(g K)).

Table 30.10 Specific heat C and Debye temperature θ_D for some III–V binaries at 300 K

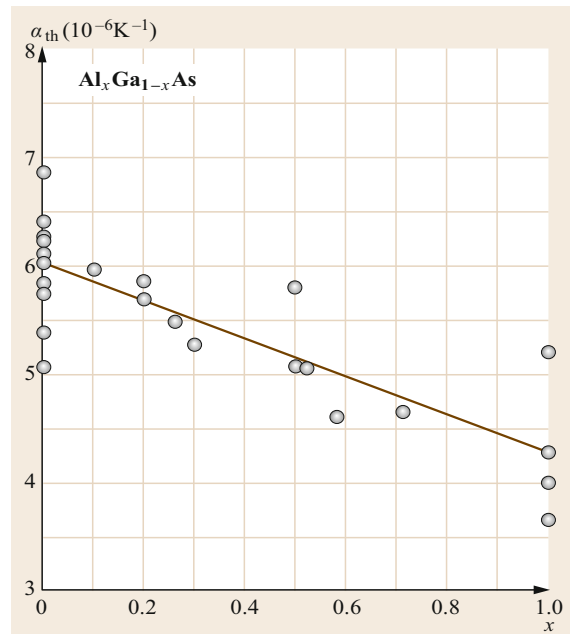| Binary	C (J/(g K))	θ_D (K)	α_{th} (10^{-6}K^{-1})
AlN	0.728	988	3.2 ($\perp c$), 2.4 ($\parallel c$)
AlP	0.727	687	
AlAs	0.424	450	4.1
AlSb	0.326[a]	370[a]	4.2
α-GaN	0.42	821	6.2 ($\perp c$), 4.9 ($\parallel c$)
GaP	0.313	493[b]	4.89
GaAs	0.327	370	5.73
GaSb	0.344[a]	240[a]	6.35
InN	2.274	674	3.830 ($\perp c$), 2.751 ($\parallel c$)
InP	0.322	420[a]	4.56
InAs	0.352	280[a]	5.50
InSb	0.350[a]	161[a]	5.04

[a] At 273 K, [b] at 150 K

Fig. 30.2 Thermal expansion coefficient α_{th} as a function of x for the $Al_xGa_{1-x}As$ ternary at $T = 300$ K. The experimental data are gathered from various sources. The *solid line* is linearly interpolated between the AlAs and GaAs values
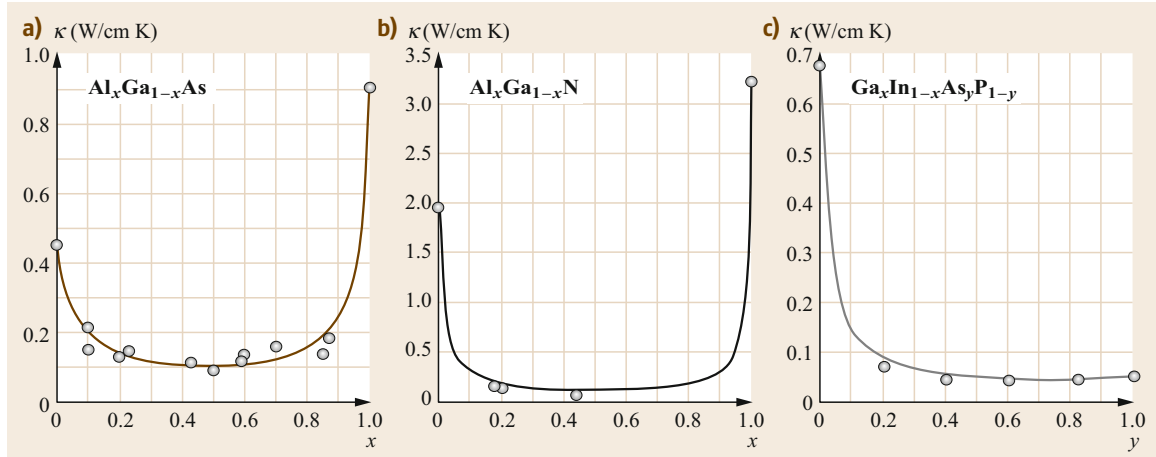
Fig. 30.3a–c Thermal conductivity κ as a function of $x(y)$ for **(a)** $Al_xGa_{1-x}As$, **(b)** $Al_xGa_{1-x}N$, and **(c)** $Ga_xIn_{1-x}As_yP_{1-y}$ lattice-matched to InP at $T = 300$ K. The experimental data (*solid circles*) are gathered from various sources. The *solid lines* represent the results calculated from (30.2) and (30.6) using the binary endpoint values and nonlinear parameters in Table 30.11

30.5.2 Thermal Expansion Coefficient

The linear thermal expansion coefficient α_{th} is usually measured by measuring the temperature dependence of the lattice parameter. The composition dependence of α_{th} has been measured for many semiconductor alloys, including $Ga_xIn_{1-x}P$ [30.15] and GaP_xAs_{1-x} [30.16]. These studies indicate that the α_{th} value varies almost linearly with composition. This suggests that the thermal expansion coefficient can be accurately estimated using linear interpolation. In fact, we plot in Fig. 30.2 the 300 K value of α_{th} as a function of x for the $Al_xGa_{1-x}As$ ternary. By using the least-squares fit procedure, we obtain the linear relationship between α_{th} and x as $\alpha_{th}(x) = 6.01 - 1.74x \, (10^{-6} \, \text{K}^{-1})$. This expression is almost the same as that obtained using the linear interpolation expression

$$\alpha_{th}(x) = 4.28x + 6.03(1-x)$$
$$= 6.03 - 1.75(10^{-6} \, \text{K}^{-1}) \ .$$

The binary endpoint values of α_{th} are listed in Table 30.10.

30.5.3 Thermal Conductivity

The lattice thermal conductivity κ, or the thermal resistivity $W = 1/\kappa$, results mainly from interactions between phonons and from the scattering of phonons by crystalline imperfections. It is important to point out that when large numbers of foreign atoms are added to the host lattice, as in alloying, the thermal conductivity may decrease significantly. Experimental data on

various alloy semiconductors, in fact, exhibit strong nonlinearity with respect to the alloy composition. Such a composition dependence can be successfully explained by using the quadratic expression of (30.2) or (30.6) [30.17].

In Fig. 30.3 we compare the results calculated from (30.2) [(30.7)] to the experimental data for $Al_xGa_{1-x}As$, $Al_xGa_{1-x}N$ and $Ga_xIn_{1-x}As_yP_{1-y}/InP$ alloys. The binary W values used in these calculations are taken from Table 30.11. The corresponding nonlinear parameters C_{A-B} are also listed in Table 30.11. The agreement between the calculated and experimen-

Table 30.11 Thermal resistivity values W for some III–V binaries at 300 K. Several cation and anion bowing parameters used for the calculation of alloy values are also listed in the last column

Binary	W (cm K/W)	C_{A-B} (cm K/W)
AlN	0.31^a	
AlP	1.11	$C_{Al-Ga} = 32$
AlAs	1.10	$C_{Al-In} = 15$
AlSb	1.75	$C_{Ga-In} = 72$
α-GaN	0.51^a	$C_{N-P} = 36$
GaP	1.30	$C_{N-As} = 12$
GaAs	2.22	$C_{N-Sb} = 10$
GaSb	2.78	$C_{P-As} = 25$
InN	2.22^b	$C_{P-Sb} = 16$
InP	1.47	$C_{As-Sb} = 91$
InAs	3.33	
InSb	5.41–6.06	

[a] Heat flow parallel to the basal plane, [b] ceramics

tal data is excellent. By applying the present model, it is possible to estimate the κ (or W) values of ex-perimentally unknown III–V alloy systems, such as $GaAs_xSb_{1-x}$ and $Al_xGa_yIn_{1-x-y}As$.

30.6 Energy Band Parameters

30.6.1 Bandgap Energy

Lowest Direct and Lowest Indirect Band Gaps

The bandgap energies of III–V ternaries usually deviate from the simple linear relation of (30.1) and have an approximately quadratic dependence on the alloy composition x. Table 30.12 summarizes the lowest direct gap energy E_0 and the lowest indirect gap energies E_g^X and E_g^L for some III–V binaries of interest here. The corresponding nonlinear parameters C_{A-B} are listed in Table 30.13 [30.18]. Note that the E_g^X and E_g^L transitions correspond to those from the highest valence band at the Γ point to the lowest conduction band near X ($\Gamma_8 \rightarrow X_6$) or near L ($\Gamma_8 \rightarrow L_6$), respectively. The E_0 transitions take place at the Γ point ($\Gamma_8 \rightarrow \Gamma_6$).

Figure 30.4 plots the values of E_0 and E_g^X as a function of alloy composition x for the $Ga_xIn_{1-x}P$ ternary at $T = 300\,\mathrm{K}$. The solid lines are obtained by introducing the numerical values from Tables 30.12 and 30.13 into (30.2). These curves provide the direct–indirect crossover composition at $x \approx 0.7$. Figure 30.5 also shows the variation in composition of E_0 in the $Ga_xIn_{1-x}As$, $InAs_xSb_{1-x}$ and $Ga_xIn_{1-x}Sb$ ternaries. It is understood from Table 30.13 that the bowing parameters for the bandgap energies of III–V ternaries are negative or very small, implying a downward bowing

or a linear interpolation to within experimental uncertainty (Figs. 30.4 and 30.5). It should be noted that nitrogen incorporation into (In,Ga)(P,As) results in a giant bandgap bowing of the host lattice for increasing nitrogen concentration [30.19]. We also summarize in Table 30.14 the expressions for the E_0 gap energy of some III–V quaternaries as a function of alloy composition.

Higher–Lying Band Gaps

The important optical transition energies observed at energies higher than E_0 are labeled E_1 and E_2. We

Table 30.12 Band-gap energies, E_0, E_g^X and E_g^L, for some III–V binaries at 300 K. ZB = zinc blende

Binary	E_0 (eV)	E_g^X (eV)	E_g^L (eV)
AlN	6.2	–	–
AlN (ZB)	5.2	5.34	8.6[a]
AlP	3.91	2.48	3.57[a]
AlAs	3.01	2.15	2.37
AlSb	2.27	1.615	2.211
α-GaN	3.420	–	–
β-GaN	3.231	4.2[a]	5.5[a]
GaP	2.76	2.261	2.63
GaAs	1.43	1.91	1.72
GaSb	0.72	1.05	0.76
InN	0.7−1.1	–	–
InN (ZB)	0.56	3.0[a]	5.8[a]
InP	1.35	2.21	2.05
InAs	0.359	1.37	1.07
InSb	0.17	1.63	0.93

[a] Theoretical

Table 30.13 Bowing parameters used in the calculation of E_0, E_g^X and E_g^L for some III–V ternaries. In those cases where no value is listed, linear variation should be assumed. W = wurtzite; ZB = zinc blende

| Ternary	Bowing parameter C_{A-B} (eV)		
	E_0	E_g^X	E_g^L
(Al,Ga)N (W)	−1.00	–	–
(Al,Ga)N (ZB)	0	−0.61	−0.80
(Al,In)N (W)	−3.70	–	–
(Al,In)N (ZB)			
(Ga,In)N (W)	−1.640	–	–
(Ga,In)N (ZB)	0		
(Al,Ga)P	0	0	
(Al,In)P	−0.40	0	
(Ga,In)P	−0.65	−0.200	−0.34
(Al,Ga)As	−0.37	−0.245	−0.055
(Al,In)As	−0.720		
(Ga,In)As	−0.580	−0.70	−0.50
(Al,Ga)Sb	−0.47	0	−0.55
(Al,In)Sb	−0.43		
(Ga,In)Sb	−0.415	−0.33	−0.40
Al(P,As)	−0.13	−0.40	−0.38
Al(P,Sb)	−2.13	−0.277	−0.756
Al(As,Sb)	−1.19	−0.250	−0.474
Ga(N,P) (ZB)	−3.9		
Ga(N,As) (ZB)	$-120.4 + 100x$		
Ga(P,As)	−0.19	−0.240	−0.16
Ga(P,Sb)	−2.70	−2.700	−2.70
Ga(As,Sb)	−1.25	−1.20	−1.20
In(N,P) (ZB)	−15		
In(N,As) (ZB)	−4.22		
In(P,As)	−0.145	−0.145	−0.145
In(P,Sb)	−1.60	−1.60	−1.60
In(As,Sb)	−0.600	−0.60	−0.60
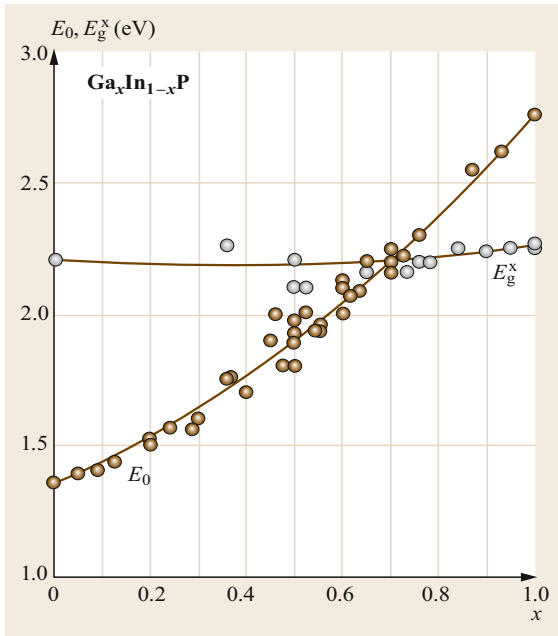
Fig. 30.4 Variation of the lowest direct gap (E_0) and lowest indirect gap energies (E_g^X) in the $Ga_xIn_{1-x}P$ ternary at $T = 300$ K. The experimental data are gathered from various sources. The *solid lines* are calculated from (30.2) using the binary endpoint values and bowing parameters in Tables 30.12 and 30.13

summarize in Table 30.15 the higher-lying bandgap energies E_1 and E_2 for some III–V binaries. The corresponding bowing parameters for these gaps are listed in Table 30.16.

30.6.2 Carrier Effective Mass

Electron Effective Mass

Since the carrier effective mass is strongly connected with the carrier mobility, it is known to be one of the most important device parameters. Effective masses can be measured by a variety of techniques, such as the Shubnikov-de Haas effect, magnetophonon resonance, cyclotron resonance, and interband magneto-optical effects. We list in Table 30.17 the electron effective mass (m_e^Γ) at the Γ-conduction band and the density of states (m_e^α) and conductivity masses (m_c^α) at the X-conduction and L-conduction bands of some III–V binaries. We also list in Table 30.18 the bowing parameters used when calculating the electron effective mass m_e^Γ for some III–V ternaries from (30.2). Note that the density of states mass m_e^α for electrons in the conduction band minima $\alpha = \Gamma$, X, and L can be obtained from

$$m_e^\alpha = N^{2/3} m_{t\alpha}^{2/3} m_{l\alpha}^{1/3} , \tag{30.16}$$

where N is the number of equivalent α minima ($N = 1$ for the Γ minimum, $N = 3$ for the X minima, and $N = 4$ for the L minima). The two masses m_l and m_t in (30.16) are called the longitudinal and transverse masses, respectively. The density of states effective mass m_e^α is used to calculate the density of states. The conductivity effective mass m_c^α, which can be used for calculating the conductivity (mobility), is also given by

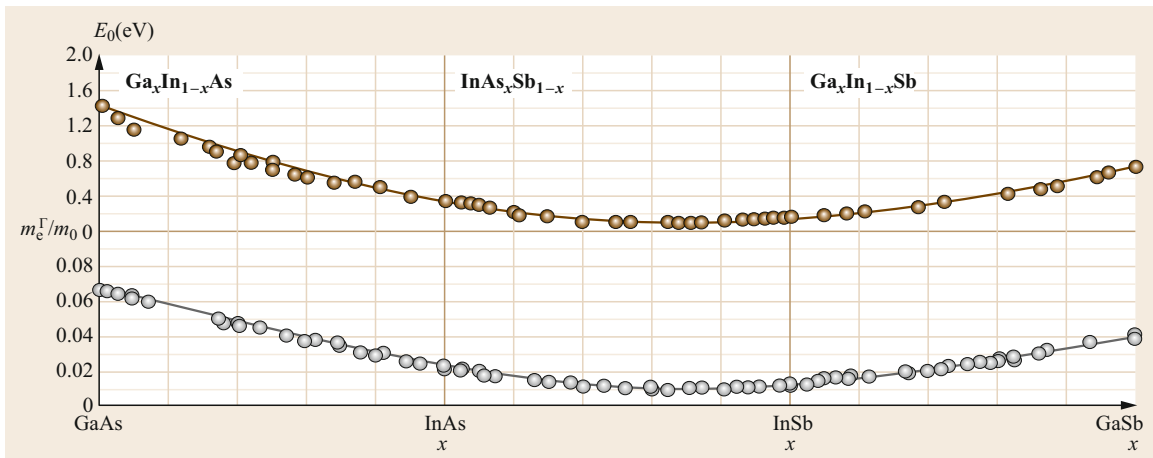$$m_c^\alpha = \frac{3 m_{t\alpha} m_{l\alpha}}{m_{t\alpha} + 2 m_{l\alpha}} . \tag{30.17}$$

Fig. 30.5 Variation of the lowest direct gap energy E_0 ($T = 300$ K) and electron effective mass m_e^Γ at the Γ-conduction bands of $Ga_xIn_{1-x}As$, $InAs_xSb_{1-x}$ and $Ga_xIn_{1-x}Sb$ ternaries. The experimental data are gathered from various sources. The *solid lines* are calculated from (30.2) using the binary endpoint values and bowing parameters in Tables 30.12 and 30.13 (E_0) and those in Tables 30.17 and 30.18 (m_e^Γ)

Table 30.14 Bandgap energies E_0 for some III–V quaternaries at 300 K

Quaternary	E_0 (eV)
$Ga_xIn_{1-x}P_yAs_{1-y}$/InP	$0.75 + 0.46y + 0.14y^2$
$Ga_xIn_{1-x}As_ySb_{1-y}$/GaSb	$0.28 - 0.16x + 0.60x^2$
$Ga_xIn_{1-x}As_ySb_{1-y}$/InAs	$0.359 - 0.415x + 0.718x^2$
$Al_xGa_yIn_{1-x-y}P$/GaAs[a]	$1.90 + 0.57x + 0.10x^2$
$Al_xGa_yIn_{1-x-y}As$/InP	$0.75 + 0.68x + 0.06x^2$
$InP_xAs_ySb_{1-x-y}$/InAs	$0.512 + 0.030y - 0.183y^2$

[a] The lowest indirect gap energy for this quaternary alloy can be obtained via $E_g^X = 2.25 + 0.09x - 0.01x^2$ eV

Table 30.15 Higher-lying bandgap energies, E_1 and E_2, for some III–V binaries at 300 K

Binary	E_1 (eV)	E_2 (eV)
AlN	7.76	8.79
AlP	4.30	4.63
AlAs	3.62–3.90	4.853, 4.89
AlSb	2.78–2.890	4.20–4.25
α-GaN	6.9	8.0
β-GaN	7.0	7.6
GaP	3.71	5.28
GaAs	2.89–2.97	4.960–5.45
GaSb	2.05	4.08–4.20
InN	5.0	7.6
InP	3.17	4.70 (E_0')
InAs	2.50	4.70
InSb	1.80	3.90

Table 30.16 Bowing parameters used in the calculation of the higher-lying bandgap energies, E_1 and E_2, for some cubic III–V ternaries. In those cases where no value is listed, linear variation should be assumed

Ternary	C_{A-B} (eV)	
	E_1	E_2 (E_0')
(Ga,In)N	−1.11	−1.26
(Al,Ga)P	0	0
(Al,In)P	0	0
(Ga,In)P	−0.86	0
(Al,Ga)As	−0.39	0
(Al,In)As	−0.44	−0.24
(Ga,In)As	−0.51	−0.27
(Al,Ga)Sb	−0.31	−0.34
(Al,In)Sb	−0.30	−0.14
(Ga,In)Sb	−0.36	−0.15
Ga(N,P)	0	0
Ga(N,As)	0	0
Ga(P,As)	0	0
Ga(As,Sb)	−0.59	−0.19
In(P,As)	−0.17	−0.03
In(As,Sb)	≈ -0.8	≈ -1.4

dependence of m_e^Γ, determined for $Ga_xIn_{1-x}P_yAs_{1-y}$ and $Al_xGa_yIn_{1-x-y}As$ quaternaries lattice-matched to InP.

Hole Effective Mass

The effective mass can only be clearly defined for an isotropic parabolic band. In the case of III–V materials, the valence bands are warped from spherical symmetry some distance away from the Brillouin zone center (Γ). Depending on the measurement or calculation technique employed, different values of hole masses are then possible experimentally or theoretically. Thus, it is always important to choose the correct definition of the effective hole mass which appropriate to the physical phenomenon considered.

We list in Table 30.20 the density of states heavy hole (m_{HH}^*), the averaged light hole (m_{LH}^*), and spin orbit splitoff effective hole masses (m_{SO}) in some cubic III–V semiconductors. These masses are, respectively, defined using Luttinger's valence band parameters γ_i by

$$m_{HH}^* = \frac{\left(1 + 0.05\gamma_h + 0.0164\gamma_h^2\right)^{2/3}}{\gamma_1 - \overline{\gamma}}, \tag{30.18}$$

$$m_{LH}^* = \frac{1}{\gamma_1 + \overline{\gamma}}, \tag{30.19}$$

$$m_{SO} = \frac{1}{\gamma_1} \tag{30.20}$$

Since $m_{t\Gamma} = m_{l\Gamma}$ at the $\alpha = \Gamma$ minimum of cubic semiconductors, we have the relation $m_e^\Gamma = m_c^\Gamma$. In the case of wurtzite semiconductors, we have the relation $m_e^\Gamma \neq m_c^\Gamma$, but the difference is very small.

The composition dependence of the electron effective mass m_e^Γ at the Γ-conduction bands of $Ga_xIn_{1-x}As$, $InAs_xSb_{1-x}$ and $Ga_xIn_{1-x}Sb$ ternaries is plotted in Fig. 30.5. The solid lines are calculated from (30.2) using the binary endpoint values and bowing parameters in Tables 30.17 and 30.18. For conventional semiconductors, the values of the effective mass are known to decrease with decreasing bandgap energy (Fig. 30.5). This is in agreement with a trend predicted by the $\mathbf{k} \cdot \mathbf{p}$ theory [30.2]. In III–V-N alloys, the electron effective mass has been predicted to increase with increasing nitrogen composition in the low composition range [30.19]. This behavior is rather unusual, and in fact is opposite to what is seen in conventional semiconductors. However, a more recent study suggested that the effective electron mass in GaN_xAs_{1-x} decreases from $0.084m_0$ to $0.029m_0$ as x increases from 0 to 0.004 [30.20]. We also summarize in Table 30.19 the composition

Table 30.17 Electron effective mass at the Γ-conduction band (m_e^Γ) and density of states (m_e^α) and conductivity masses (m_c^α) at the X-conduction and L-conduction bands of some III–V binaries. ZB = zinc blende

Binary	m_e^Γ/m_0	Density of states mass		Conductivity mass	
		m_e^X/m_0	m_e^L/m_0	m_c^X/m_0	m_c^L/m_0
AlN	0.29−0.45	–	–	–	–
AlN (ZB)	0.26[a]	0.78[a]		0.37[a]	
AlP	0.220[a]	1.14[a]		0.31[a]	
AlAs	0.124	0.71	0.78	0.26[a]	0.21[a]
AlSb	0.14	0.84	1.05[a]	0.29	0.28[a]
α-GaN	0.21	–	–	–	–
β-GaN	0.15	0.78[a]		0.36[a]	
GaP	0.114	1.58	0.75[a]	0.37	0.21[a]
GaAs	0.067	0.85	0.56	0.32	0.11
GaSb	0.039	1.08[a]	0.54	0.44[a]	0.12
InN	0.044	–	–	–	–
InN (ZB)	0.03[a]				
InP	0.07927	1.09[a]	0.76[a]	0.45[a]	0.19[a]
InAs	0.024	0.98[a]	0.94[a]	0.38[a]	0.18[a]
InSb	0.013				

[a] Theoretical

Table 30.18 Bowing parameter used in the calculation of the electron effective mass m_e^Γ at the Γ-conduction bands of some III–V ternaries

Ternary	C_{A-B} (m_0)
(Ga,In)P	−0.01854
(Al,Ga)As	0
(Al,In)As	−0.012
(Ga,In)As	−0.008
(Ga,In)Sb	−0.010
Ga(P,As)	0
Ga(As,Sb)	−0.014
In(P,As)	0
In(As,Sb)	−0.027

with

$$\overline{\gamma} = \left(2\gamma_2^2 + 2\gamma_3^2\right)^{1/2} , \quad \gamma_h = \frac{6\left(\gamma_3^2 - \gamma_2^2\right)}{\overline{\gamma}(\gamma_1 - \overline{\gamma})} .$$

(30.21)

Only a few experimental studies have been performed on the effective hole masses in III–V alloys, e.g., the $Ga_xIn_{1-x}P_yAs_{1-y}$ quaternary [30.2]. While some data imply a bowing parameter, the large uncertainties in existing determinations make it difficult to conclusively state that such experimental values are preferable to a linear interpolation. The binary endpoint data listed in Table 30.20 enable us to estimate alloy values using the linear interpolation scheme.

30.6.3 Deformation Potential

The deformation potentials of the electronic states at the Brillouin zone centers of semiconductors play an im-

Table 30.19 Electron effective mass m_e^Γ at the Γ-conduction bands of some III–V quaternaries

Quaternary	m_e^Γ/m_0
$Ga_xIn_{1-x}P_yAs_{1-y}$/InP	$0.04084 + 0.03384y + 0.00459y^2$
$Al_xGa_yIn_{1-x-y}As$/InP	$0.043 + 0.031x$

Table 30.20 Density of states heavy hole (m_{HH}^*), averaged light hole (m_{LH}^*), and spin orbit splitoff effective hole masses (m_{SO}) in some cubic III–V semiconductors. ZB = zinc blende

Material	m_{HH}^*/m_0	m_{LH}^*/m_0	m_{SO}/m_0
AlN (ZB)	1.77[a]	0.35[a]	0.58[a]
AlP	0.63[a]	0.20[a]	0.29[a]
AlAs	0.81[a]	0.16[a]	0.30[a]
AlSb	0.9	0.13	0.317[a]
β-GaN	1.27[a]	0.21[a]	0.35[a]
GaP	0.52	0.17	0.34
GaAs	0.55	0.083	0.165
GaSb	0.37	0.043	0.12
InN (ZB)	1.959[a]	0.098[a]	0.186[a]
InP	0.69	0.11	0.21
InAs	0.36	0.026	0.14
InSb	0.38	0.014	0.10

[a] Theoretical

portant role in many physical phenomena. For example, the splitting of the heavy hole and light hole bands at the Γ point of the strained substance can be explained by the shear deformation potentials, b and d. The lattice mobilities of holes are also strongly affected by these potentials. Several experimental data have been

Table 30.21 Conduction-band (a_c) and valence-band deformation potentials (a_v, b, d) for some cubic III–V binaries. ZB = zinc blende

Binary	Conduction band	Valence band		
	a_c (eV)	a_v (eV)	b (eV)	d (eV)
AlN (ZB)	−11.7[a]	−5.9[a]	−1.7[a]	−4.4[a]
AlP	−5.54[a]	3.15[a]	−1.5[a]	
AlAs	−5.64[a]	−2.6[a]	−2.3[a]	
AlSb	−6.97[a]	1.38[a]	−1.35	−4.3
β-GaN	−21.3[a]	−13.33[a]	−2.09[a]	−1.75[a]
GaP	−7.14[a]	1.70[a]	−1.7	−4.4
GaAs	−11.0	−0.85	−1.85	−5.1
GaSb	−9	0.79[a]	−2.4	−5.4
InP	−11.4	−0.6	−1.7	−4.3
InAs	−10.2	1.00[a]	−1.8	−3.6
InSb	−15	0.36[a]	−2.0	−5.4

[a] Theoretical

Table 30.22 Conduction-band (D_i) and valence-band deformation potentials (C_i) for some wurtzite III–V binaries (in eV)

Binary	Conduction band		Valence band							
	D_1	D_2	C_1	D_1–C_1	C_2	D_2–C_2	C_3	C_4	C_5	C_6
AlN	−10.23[a]	−9.65[a]	−12.9[a]		−8.4[a]		4.5[a]	−2.2[a]	−2.6[a]	−4.1[a]
α-GaN	−9.47[a]	−7.17[a]	−41.4	−3.1	−33.3	−11.2	8.2	−4.1	−4.7	
InN			−4.05[a]		−6.67[a]		4.92[a]	−1.79[a]		

[a] Theoretical

reported on the deformation potential values for III–V alloys, $Al_xGa_{1-x}As$ [30.12], GaP_xAs_{1-x} [30.21] and $Al_xIn_{1-x}As$ [30.22]. Due to the large scatter in the experimental binary endpoint values, it is very difficult to establish any evolution of the deformation potentials with composition. We list in Table 30.21 the recommended values for the conduction band (a_c) and valence

band deformation potentials (a_v, b, d) of some cubic III–V binaries. The deformation potentials for some wurtzite III–V semiconductors are also collected in Table 30.22. Until more precise data become available, we suggest employing the linear interpolation expressions in order to estimate the parameter values of these poorly explored properties.

30.7 Optical Properties

30.7.1 The Reststrahlen Region

It should be noted that in homopolar semiconductors like Si and Ge, the fundamental vibration has no dipole moment and is infrared inactive. In heteropolar semiconductors, such as GaAs and InP, the first-order dipole moment gives rise to a very strong absorption band associated with optical modes that have a $\boldsymbol{k}$ vector of essentially zero (i. e., long-wavelength optical phonons). This band is called the reststrahlen band. Below this band, the real part of the dielectric constant asymptotically approaches the static or low-frequency dielectric constant ε_s. The optical constant connecting the reststrahlen near-infrared spectral range is called the high-frequency or optical dielectric constant ε_∞. The

value of ε_∞ is, therefore, measured for frequencies well above the long-wavelength LO phonon frequency but below the fundamental absorption edge.

The general properties of ε_s and ε_∞ for a specific family of compounds, namely III–V and II–VI compounds, suggest that the dielectric constants in alloy semiconductors could be deduced by using the linear interpolation method [30.26]. The simplest linear interpolation method is to use (30.1), (30.3) or (30.5). The linear interpolation scheme based on the Clausius–Mosotti relation can also be obtained from (30.6). In Fig. 30.6, we show the interpolated ε_∞ as a function of x for the $Al_xGa_{1-x}Sb$ ternary. The solid and dashed lines are, respectively, calculated from (30.1) and (30.6) (ternary). The experimental data are taken from *Lu-*
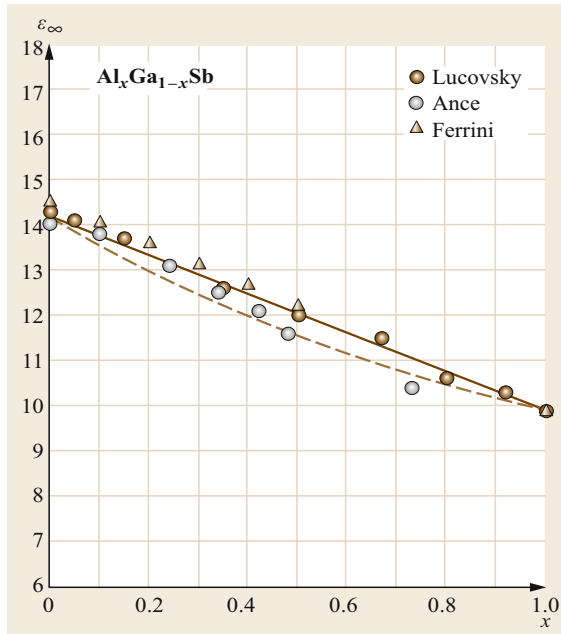
Fig. 30.6 High-frequency dielectric constant ε_∞ as a function of x for the $Al_xGa_{1-x}Sb$ ternary. The experimental data are taken from *Lucovsky* et al. [30.23] (*solid circles*), *Ance* and *Van Mau* [30.24] (*open circles*), and *Ferrini* et al. [30.25] (*open triangles*). The *solid* and *dashed lines* are, respectively, calculated from (30.1) and (30.6) (ternary) with the binary endpoint values in Table 30.23

Table 30.23 Static (ε_s) and high-frequency dielectric constants (ε_∞) for some cubic III–V binaries. ZB = zinc blende

Binary	ε_s	ε_∞
AlN (ZB)	8.07[a]	4.25
AlP	9.6	7.4
AlAs	10.06	8.16
AlSb	11.21	9.88
β-GaN	9.40[a]	5.35[a]
GaP	11.0	8.8
GaAs	12.90	10.86
GaSb	15.5	14.2
InN (ZB)	12.2[a]	7.92[a]
InP	12.9	9.9
InAs	14.3	11.6
InSb	17.2	15.3

[a] Calculated or estimated

covsky et al. [30.23], *Ance* and *Van Mau* [30.24], and *Ferrini* et al. [30.25]. The binary endpoint values used in the calculation are listed in Table 30.23. These two methods are found to provide almost the same interpolated values. Table 30.24 also lists the ε_s and ε_∞
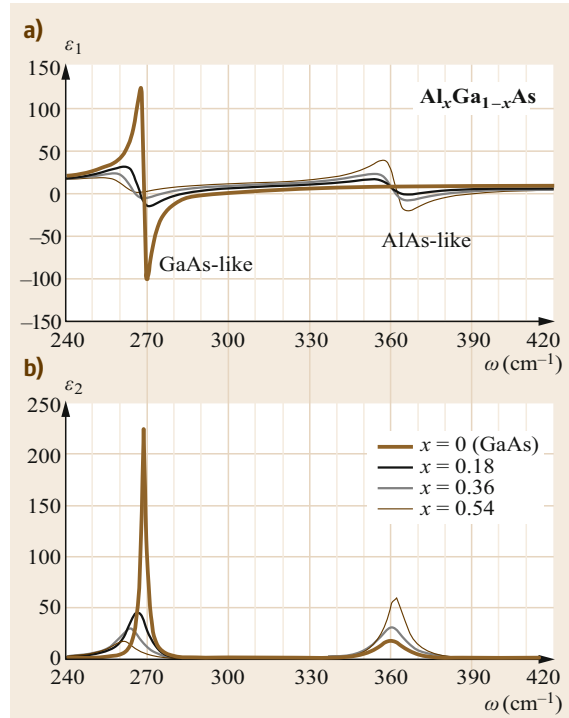

Fig. 30.7 $\varepsilon(\omega)$ spectra in the reststrahlen region of the $Al_xGa_{1-x}As$ ternary

Table 30.24 Static (ε_s) and high-frequency dielectric constants (ε_∞) for some wurtzite III–V binaries

Binary	$E \perp c$		$E \parallel c$	
	ε_s	ε_∞	ε_s	ε_∞
AlN	8.3	4.4	8.9	4.8
α-GaN	9.6	5.4	10.6	5.4
InN	10.6[a]	7.03[a]	12.3[a]	7.41[a]

[a] Estimated

values for some wurtzite III–V binary semiconductors.

The optical spectra observed in the reststrahlen region of alloy semiconductors can be explained by the following multioscillator model [30.12]

$$\varepsilon(\omega) = \varepsilon_\infty + \sum_j \frac{S_j \omega_{TOj}^2}{\omega_{TOj}^2 - \omega^2 - i\omega\gamma_j} , \qquad (30.22)$$

where $S_j = \varepsilon_\infty (\omega_{LOj}^2 - \omega_{TOj}^2)$ is the oscillator strength, ω_{TOj} (ω_{LOj}) is the TO (LO) phonon frequency, and γ_j is the damping constant of the j-th lattice oscillator. We show in Fig. 30.7, as an example, the optical spectra in the reststrahlen region of the $Al_xGa_{1-x}As$ ternary. As expected from the two-mode behavior of the long-wavelength optical phonons, the $\varepsilon(\omega)$ spec-

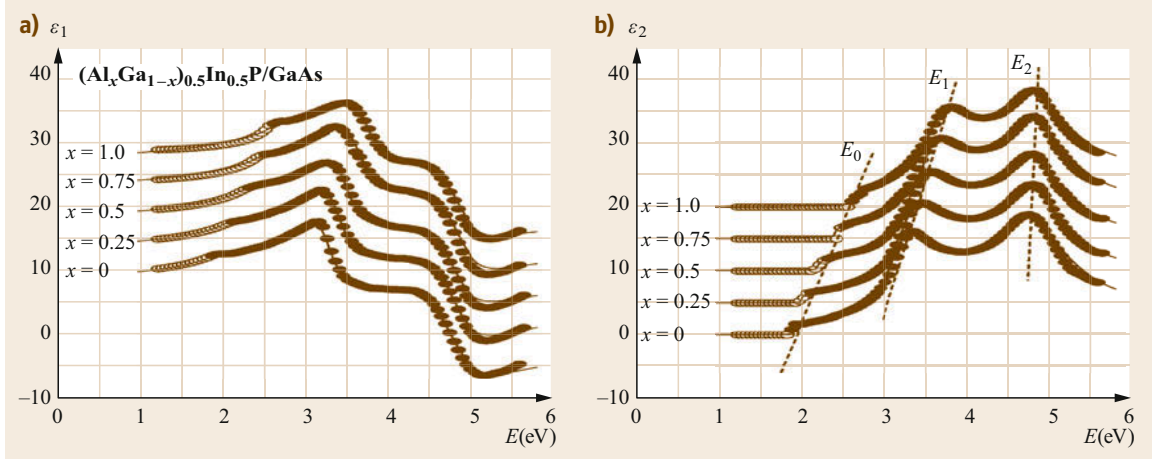**Fig. 30.8a,b** $\varepsilon(E)$ spectra for $Al_xGa_yIn_{1-x-y}P/GaAs$ at room temperature. The experimental data are taken from *Adachi* [30.27]; *open* and *solid circles*. The *solid lines* represent the theoretical fits for the MDF calculation

tra of $Al_xGa_{1-x}As$ exhibit two main optical resonances: GaAs-like and AlAs-like.

30.7.2 The Interband Transition Region

The optical constants in the interband transition regions of semiconductors depend fundamentally on the electronic energy band structure of the semiconductors. The relation between the electronic energy band structure and $\varepsilon_2(E)$ is given by

$$\varepsilon_2(E) = \frac{4e^2\hbar^2}{\pi\mu^2E^2} \int d\boldsymbol{k} \, |P_{cv}(\boldsymbol{k})|^2 \, \delta[E_c(k)-E_v(k)-E] \,, \tag{30.23}$$

where μ is the combined density of states mass, the Dirac δ function represents the spectral joint density of states between the valence-band $[E_v(\boldsymbol{k})]$ and conduction-band states $[E_c(\boldsymbol{k})]$, differing by the energy $E = \hbar\omega$ of the incident light, $P_{cv}(\boldsymbol{k})$ is the momentum matrix element between the valence-band and conduction-band states, and the integration is performed over the first Brillouin zone. The Kramers–Kronig relations link $\varepsilon_2(E)$ and $\varepsilon_1(E)$ in a manner that

means that $\varepsilon_1(E)$ can be calculated at each photon energy if $\varepsilon_2(E)$ is known explicitly over the entire photon energy range, and vice versa. The Kramers–Kronig relations are of fundamental importance in the analysis of optical spectra [30.9].

The refractive indices and absorption coefficients of semiconductors are the basis of many important applications of semiconductors, such as light-emitting diodes, laser diodes and photodetectors. The optical constants of III–V binaries and their ternary and quaternary alloys have been presented in tabular and graphical forms [30.27]. We plot in Fig. 30.8 the $\varepsilon(E)$ spectra for $Al_xGa_yIn_{1-x-y}P/GaAs$ taken from tabulation by *Adachi* ([30.27]; open and solid circles). The solid lines represent the theoretical fits of the model dielectric function (MDF) calculation [30.9]. The three major features of the spectra seen in Fig. 30.8 are the E_0, E_1 and E_2 structures at ≈ 2, ≈ 3.5 and $\approx 4.5\,\text{eV}$, respectively. It is found that the E_0 and E_1 structures move to higher energies with increasing x, while the E_2 structure does not do so to any perceptible degree. We can see that the MDF calculation enables us to calculate the optical spectra for optional compositions of alloy semiconductors with good accuracy.

30.8 Carrier Transport Properties

An accurate comparison between experimental mobility and theoretical calculation is of great importance for the determination of a variety of fundamental material parameters and carrier scattering mechanisms. There are various carrier scattering mechanisms in semiconductors, as schematically shown in Fig. 30.9. The effect

of the individual scattering mechanisms on the total calculated carrier mobility can be visualized using Matthiessen's rule:

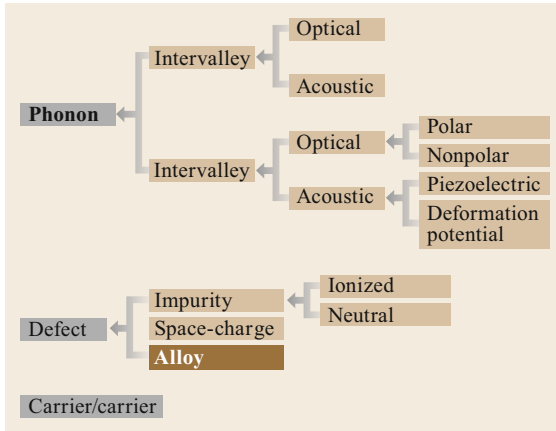$$\frac{1}{\mu_{tot}} = \sum_i \frac{1}{\mu_i} \,. \tag{30.24}$$

Fig. 30.9 Various possible carrier scattering mechanisms in semiconductor alloys

Table 30.25 Hall mobilities for electrons (μ_e) and holes (μ_h) obtained at 300 K for relatively pure samples of III–V binaries (in cm^2/(V s))

Binary	μ_e	μ_h
AlN	125	14
AlP	80	450
AlAs	294	105
AlSb	200	420
α-GaN	1245	370
β-GaN	760	350
GaP	189	140
GaAs	9340	450
GaSb	12 040	1624
InN	3100	39
InP	6460	180
InAs	33 000	450
InSb	77 000	1100

The total carrier mobility μ_{tot} can then be obtained from the scattering-limited mobilities μ_i of each scattering mechanism. We note that in alloy semiconductors the charged carriers see potential fluctuations as a result of the composition disorder. This kind of scattering mechanism, so-called alloy scattering, is important in some III–V ternaries and quaternaries. The alloy scattering limited mobility in ternary alloys can be formulated as

$$\mu_{al} = \frac{\sqrt{2\pi}e\hbar^4 N_{al}\alpha}{3(m_c^*)^{5/2}(kT)^{1/2}x(1-x)(\Delta U)^2} , \qquad (30.25)$$

where N_{al} is the density of alloy sites, m_c^* is the electron or hole conductivity mass, x and $(1-x)$ are the mole fractions of the binary endpoint materials, and ΔU is the alloy scattering potential. The factor α is caused by

the band degeneracy and is given by $\alpha = 1$ for electrons and by $\alpha = [(d^{5/2}+d^3)/(1+d^{3/2})^2]$ for holes with $d = m_{HH}/m_{LH}$, where m_{HH} and m_{LH} are the heavy hole and light hole band masses, respectively [30.12].

Let us simply express the total carrier mobility μ_{tot} in alloy $A_xB_{1-x}C$ as

$$\frac{1}{\mu_{tot}(x)} = \frac{1}{x\mu_{tot}(AC) + (1-x)\mu_{tot}(BC)} + \frac{1}{\mu_{al,0}/\frac{x}{1-x}} . \qquad (30.26)$$

The first term in (30.26) comes from the linear interpolation scheme and the second term accounts for the effects of alloying.
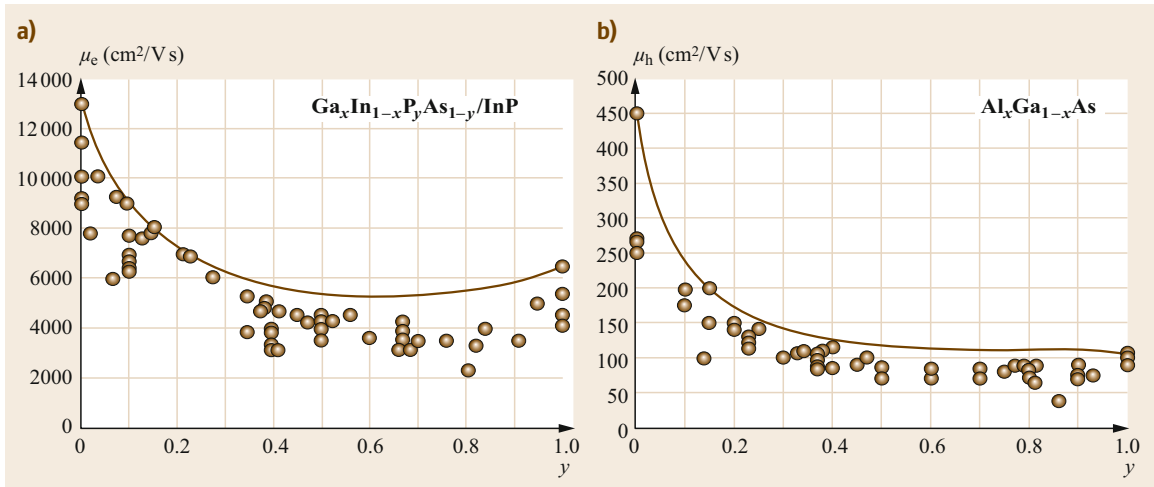

Fig. 30.10 (a) Electron Hall mobility μ_e in the $Ga_xIn_{1-x}P_y As_{1-y}$/InP quaternary and **(b)** the hole Hall mobility μ_h in the $Al_xGa_{1-x}As$ ternary, respectively. The experimental data correspond to those for relatively pure samples. The *solid lines* in **(a)** and **(b)** represent the results calculated using (30.26) with $\mu_{al,0} = 3000$ and 50 cm^2/(V s), respectively

We plot in Figs. 30.10a and 30.10b the electron Hall mobility in the $Ga_xIn_{1-x}P_yAs_{1-y}$/InP quaternary (μ_e) and the hole Hall mobility in the $Al_xGa_{1-x}As$ ternary, respectively. The experimental data correspond to those for relatively pure samples [30.28]. The solid lines in Figs. 30.10a,b represent the results calculated using (30.26) with $\mu_{al,0} = 3000$ and $50\,cm^2/(V\,s)$, respectively. The corresponding binary endpoint values for μ_{tot} are listed in Table 30.25. For $Ga_xIn_{1-x}P_yAs_{1-y}$/InP, we have considered the quaternary to be an alloy of the constituents $Ga_{0.53}In_{0.47}As$ ($y = 0$) and InP ($y = 1.0$) and we have used the value of μ_{tot} ($Ga_{0.47}In_{0.53}As$) $= 13\,000\,cm^2/(V\,s)$. It is clear that (30.26) can successfully explain the peculiar composition dependence of the carrier mobility in the semiconductor alloys.

References

30.1   A. Mascarenhas: *Spontaneous Ordering in Semiconductor Alloys* (Kluwer, New York 2002)
30.2   S. Adachi: *Physical Properties of III–V Semiconductor Compounds: InP, InAs, GaAs, GaP, InGaAs, and InGaAsP* (Wiley–Interscience, New York 1992)
30.3   S. Adachi: *Handbook on Physical Properties of Semiconductors*, III–V Compound Semiconductors, Vol. 2 (Springer, Berlin, Heidelberg 2004)
30.4   W. Martienssen (Ed.): *Landolt–Börnstein, Group III/41 Semiconductors, A1α Lattice Parameters* (Springer, Berlin, Heidelberg 2001)
30.5   D.Y. Watts, A.F.W. Willoughby: J. Appl. Phys. **56**, 1869 (1984)
30.6   D. Cáceres, I. Vergara, R. González, E. Monroy, F. Calle, E. Muñoz, F. Omnès: J. Appl. Phys. **86**, 6773 (1999)
30.7   M. Krieger, H. Sigg, N. Herres, K. Bachem, K. Köhler: Appl. Phys. Lett. **66**, 682 (1995)
30.8   W.E. Hoke, T.D. Kennedy, A. Torabi: Appl. Phys. Lett. **79**, 4160 (2001)
30.9   S. Adachi: *Optical Properties of Crystalline and Amorphous Semiconductors: Materials and Fundamental Principles* (Kluwer, Boston 1999)
30.10   C. Pickering: J. Electron. Mater. **15**, 51 (1986)
30.11   D.H. Jaw, Y.T. Cherng, G.B. Stringfellow: J. Appl. Phys. **66**, 1965 (1989)
30.12   S. Adachi: *GaAs and Related Materials: Bulk Semiconducting and Superlattice Properties* (World Scientific, Singapore 1994)
30.13   A.N.N. Sirota, A.M. Antyukhov, V.V. Novikov, V.A. Fedorov: Sov. Phys. Dokl. **26**, 701 (1981)
30.14   J.L. Pichardo, J.J. Alvarado-Gil, A. Cruz, J.G. Mendoza, G. Torres: J. Appl. Phys. **87**, 7740 (2000)
30.15   I. Kudman, R.J. Paff: J. Appl. Phys. **43**, 3760 (1972)
30.16   J. Bąk-Misiuk, H.G. Brühl, W. Paszkowicz, U. Pietsch: Phys. Status Solidi (a) **106**, 451 (1988)
30.17   S. Adachi: J. Appl. Phys. **54**, 1844 (1983)
30.18   I. Vurgaftman, J.R. Meyer, L.R. Ram-Mohan: J. Appl. Phys. **89**, 5815 (2001)
30.19   I.A. Buyanova, W.M. Chen, B. Monemar: MRS Internet J. Nitride Semicond. Res. **6**, 2 (2001)
30.20   D.L. Young, J.F. Geisz, T.J. Coutts: Appl. Phys. Lett. **82**, 1236 (2003)
30.21   Y. González, G. Armelles, L. González: J. Appl. Phys. **76**, 1951 (1994)
30.22   L. Pavesi, R. Houdré, P. Giannozzi: J. Appl. Phys. **78**, 470 (1995)
30.23   G. Lucovsky, K.Y. Cheng, G.L. Pearson: Phys. Rev. B **12**, 4135 (1975)
30.24   C. Ance, N. Van Mau: J. Phys. C **9**, 1565 (1976)
30.25   R. Ferrini, M. Galli, G. Guizzetti, M. Patrini, A. Bosacchi, S. Franchi, R. Magnanini: Phys. Rev. B **56**, 7549 (1997)
30.26   S. Adachi: J. Appl. Phys. **53**, 8775 (1982)
30.27   S. Adachi: *Optical Constants of Crystalline and Amorphous Semiconductors: Numerical Data and Graphical Information* (Kluwer, Boston 1999)
30.28   M. Sotoodeh, A.H. Khalid, A.A. Rezazadeh: J. Appl. Phys. **87**, 2890 (2000)